

This is an Open Access document downloaded from ORCA, Cardiff University's institutional repository: <https://orca.cardiff.ac.uk/id/eprint/165887/>

This is the author's version of a work that was submitted to / accepted for publication.

Citation for final published version:

Harding, Edward, Araki, Tohru, Askey, Joseph, Hunt, Matthew, Van Den Berg, Arjen, Raftrey, David, Aballe, Lucia, Kaulich, Burkhard, MacDonald, Emyr, Fischer, Peter and Ladak, Sam 2024. Imaging the magnetic nanowire cross-section and magnetic ordering within a suspended 3D artificial spin-ice. *APL Materials* 12, 021116. 10.1063/5.0176907

Publishers page: <https://doi.org/10.1063/5.0176907>

Please note:



Changes made as a result of publishing processes such as copy-editing, formatting and page numbers may not be reflected in this version. For the definitive version of this publication, please refer to the published source. You are advised to consult the publisher's version if you wish to cite this paper.

This version is being made available in accordance with publisher policies. See <http://orca.cf.ac.uk/policies.html> for usage policies. Copyright and moral rights for publications made available in ORCA are retained by the copyright holders.



RESEARCH ARTICLE | FEBRUARY 14 2024

Imaging the magnetic nanowire cross section and magnetic ordering within a suspended 3D artificial spin-ice

Edward Harding ; Tohru Araki; Joseph Askey ; Matthew Hunt; Arjen Van Den Berg ; David Raftrey ; Lucia Aballe ; Burkhard Kaulich ; Emyr MacDonald ; Peter Fischer ; Sam Ladak  



APL Mater. 12, 021116 (2024)

<https://doi.org/10.1063/5.0176907>

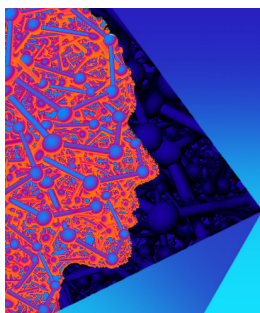


View
Online



Export
Citation

28 March 2024 14:55:48



APL Materials

Special Topic: 2D Materials for Biomedical Applications

Submit Today



Imaging the magnetic nanowire cross section and magnetic ordering within a suspended 3D artificial spin-ice

Cite as: APL Mater. 12, 021116 (2024); doi: 10.1063/5.0176907

Submitted: 18 September 2023 • Accepted: 18 January 2024 •

Published Online: 14 February 2024



Edward Harding,¹ Tohru Araki,^{2,3} Joseph Askey,¹ Matthew Hunt,¹ Arjen Van Den Berg,¹ David Raftrey,^{4,5} Lucia Aballe,⁶ Burkhard Kaulich,³ Emyr MacDonald,¹ Peter Fischer,^{4,5} and Sam Ladak^{1,a)}

AFFILIATIONS

¹ School of Physics and Astronomy, Cardiff University, Cardiff CF24 3AA, United Kingdom

² UVSOR Synchrotron Facility, Institute for Molecular Science, Okazaki 444-8585, Japan

³ Diamond Light Source Ltd., Harwell Science and Innovation Campus, Chilton OX11 0DE, United Kingdom

⁴ Materials Sciences Division, Lawrence Berkeley National Laboratory, Berkeley, California 94720, USA

⁵ Physics Department, University of California Santa Cruz, Santa Cruz, California 95064, USA

⁶ Alba Synchrotron Light Facility, Cerdanyola del Valles, Barcelona 08290, Spain

^{a)} Author to whom correspondence should be addressed: ladaks@cardiff.ac.uk

ABSTRACT

Artificial spin-ice systems are patterned arrays of magnetic nanoislands arranged into frustrated geometries and provide insight into the physics of ordering and emergence. The majority of these systems have been realized in two-dimensions, mainly due to the ease of fabrication, but with recent developments in advanced nanolithography, three-dimensional artificial spin ice (ASI) structures have become possible, providing a new paradigm in their study. Such artificially engineered 3D systems provide new opportunities in realizing tunable ground states, new domain wall topologies, monopole propagation, and advanced device concepts, such as magnetic racetrack memory. Direct imaging of 3DASI structures with magnetic force microscopy has thus far been key to probing the physics of these systems but is limited in both the depth of measurement and resolution, ultimately restricting measurement to the uppermost layers of the system. In this work, a method is developed to fabricate 3DASI lattices over an aperture using two-photon lithography, thermal evaporation, and oxygen plasma exposure, allowing the probe of element-specific structural and magnetic information using soft x-ray microscopy with x-ray magnetic circular dichroism (XMCD) as magnetic contrast. The suspended polymer-permalloy lattices are found to be stable under repeated soft x-ray exposure. Analysis of the x-ray absorption signal allows the complex cross section of the magnetic nanowires to be reconstructed and demonstrates a crescent-shaped geometry. Measurement of the XMCD images after the application of an in-plane field suggests a decrease in magnetic moment on the lattice surface due to oxidation, while a measurable signal is retained on sub-lattices below the surface.

© 2024 Author(s). All article content, except where otherwise noted, is licensed under a Creative Commons Attribution (CC BY) license (<http://creativecommons.org/licenses/by/4.0/>). <https://doi.org/10.1063/5.0176907>

The study of three-dimensional (3D) magnetic nanostructures is a rapidly growing research area^{1–4} due to their potential technological applications^{5,6} and emerging fundamental physics driven by non-trivial geometry and topology,^{7–9} as well as the frustration that can arise due to the interaction between 3D nanoelements.^{10–14} Advances in theory have shown that curvature and torsion can yield additional energy terms in the form of effective Dzyaloshinskii–Moriya and effective anisotropy interactions.^{15–17}

Such interactions can lead to the stabilization of topological spin textures^{18–20} without the need for multilayer systems and can also yield novel dynamic phenomena, such as domain wall automation.²¹ Advancements in complex fabrication processes have allowed the realization of many 3D geometries, including cylindrical magnetic nanowires,²² rolled up membranes,²³ helical structures,^{24,25} and 3D artificial spin-ice structures,¹² by harnessing a range of self-assembly and lithographic methods. Next-generation magnetic racetrack

memories⁵ rely upon 3D architectures, and before such technologies can be realized, the detailed physics of domain wall topology, propagation, and pinning needs to be understood in magnetic nanowires and elements of complex geometry. Advances in nanofabrication, theoretical modeling, and advanced characterization to validate such systems are a prerequisite in that regard.

Of the many fabrication methodologies available, direct-write technologies are particularly interesting since they provide the most freedom in the choice of geometry. Such technologies can harness either photons²⁶ or electrons^{27,28} to generate the desired 3D geometry. For example, focused electron beam-induced deposition (FEBID) has been used to realize magnetic nanowires with transfer of domain walls from a planar substrate to an angled 3D nanowire²⁹ and exotic double helix structures that generate topological defects in the stray field.⁹ Two-photon lithography (TPL) is a methodology whereby 3D nanostructures can be written by design within a suitable negative-tone photoresist by scanning a tightly focused laser through the resist to achieve the desired geometry.²⁶ The technique has been used in combination with deposition technologies to create bucky ball structures,^{30,31} magnetic nanowires,¹¹ 3D artificial

spin-ice (3DASI) building blocks,³² and arrays.^{10,12} To characterize 3DASI array systems, magnetic force microscopy (MFM) was used to directly image the propagation of monopoles across the lattice¹² and to image the demagnetized state, suggesting relaxation into an exotic magnetic charge crystal. However, a key limitation of MFM is the requirement to physically access the surface topography to obtain accurate magnetic information, a challenging feat for any 3D lattice. The resolution of MFM depends upon the lift height, which is usually limited to 50–100 nm. It is, therefore, expected that advanced characterization techniques using polarized x-ray spectro-microscopies for tomographic reconstructions, with sub-50 nm resolution, will become important in measuring next-generation 3D magnetic nanostructures.^{1,2,9,33,34}

In this article, we develop a new fabrication process that yields suspended 3DASI systems over an aperture. This allows measurement of full lattices with optical access to all nanowires without any need for tilt or rotation, while also eliminating any sheet film under the 3D nanostructure, in principle allowing the ordering to be determined. The element specific 3D geometric cross section of underlying nanowires is determined, and x-ray magnetic circular

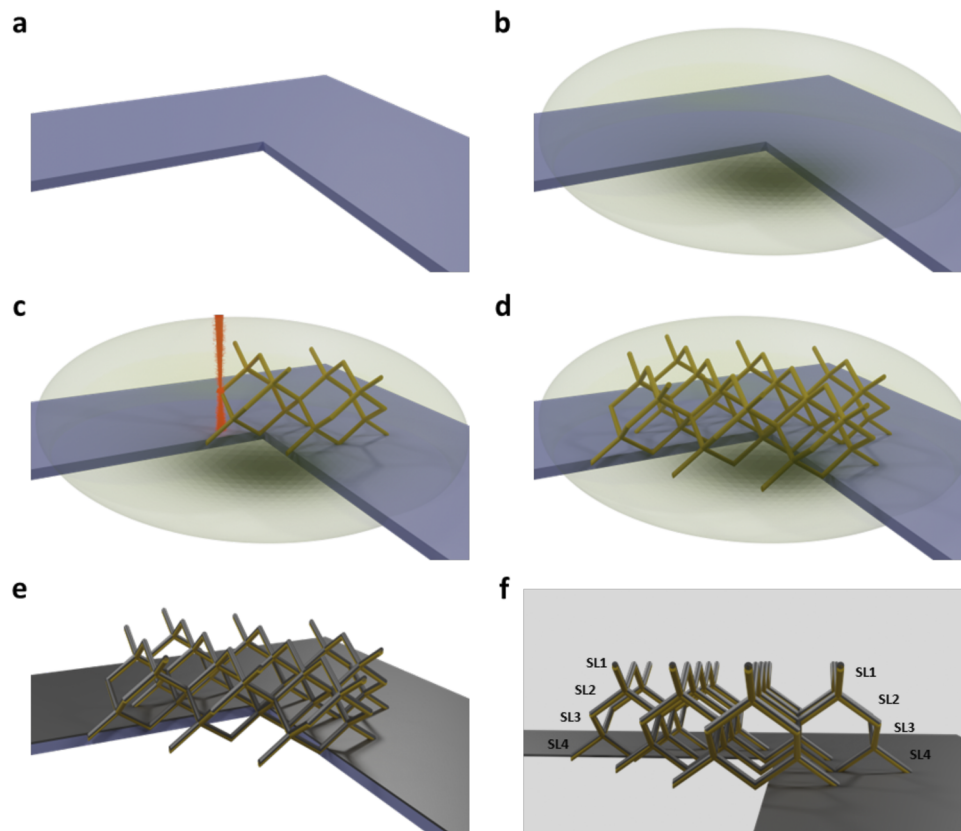


FIG. 1. Fabrication methodology for suspended 3DASI. (a) A Si substrate with an aperture of $50 \times 50 \mu\text{m}^2$ is cleaned. (b) Surface of the Si substrate is coated with a negative-tone resist (IP DIP). In panels (c) and (d), two-photon lithography is used to polymerize the resist in a diamond bond lattice geometry ($12 \times 30 \times 2.3 \mu\text{m}^3$) over the aperture corner. (e) Sample development and cleaning in IPA removes the unexposed resist and reveals a solid polymer scaffold structure. Permalloy ($\text{Ni}_{81}\text{Fe}_{19}$) is deposited onto the upper surface of the lattice via thermal evaporation, resulting in a suspended 3DASI structure. (f) Schematic showing the final structure with individual sub-lattices SL1, SL2, SL3, and SL4, upon the 3DASI.

dichroism (XMCD) shows evidence of a magnetic signal, allowing the magnetic texture upon a single sub-lattice to be reconstructed.

TPL is used to realize a diamond-bond polymer lattice over the exposed corner of a $50 \times 50 \mu\text{m}^2$ Si aperture (Silson TEM-200-0.05-aperture). Crucially, the use of a dip-in TPL technique allows the structure to be firmly anchored upon a large region of a Si substrate, providing support for the suspended lattice region. Figure 1 shows a schematic of the fabrication process. The Si substrate is first cleaned in acetone and isopropyl alcohol (IPA) and then carefully dried using compressed air [Fig. 1(a)]. A negative-tone photoresist (IP dip, Nanoscribe) is drop-cast onto the Si substrate and loaded into a TPL apparatus [Fig. 1(b)]. A diamond-bond lattice, one unit cell in height ($\sim 2.3 \mu\text{m}$), is written across each corner of the aperture [Figs. 1(c) and 1(d)], after which the sample is developed in propylene glycol monomethyl ether acetate (PGMEA), rinsed in IPA, and then carefully dried using compressed air [Fig. 1(e)]. Figure 1(f) shows a schematic of a final structure with sub-lattice layers labeled SL1–SL4. The SL1 nanowire layer is the upper surface termination and consists of coordination two and coordination four vertices. Layers SL2 and SL3 are comprised entirely of coordination four vertices. The SL4 wire layer is akin to SL1 with alternating coordination two and coordination four vertices.

Two sample sets were produced to investigate the extent to which a lattice can be suspended over an aperture. In sample set A, TPL was used with piezoelectric stages, scanning the sample with respect to the point of focus and only with an exposure of sub-lattices SL1 and SL2. In the second sample set, galvanometric mirrors were used to steer the laser focus with respect to the sample, with full exposure of sub-lattices L1–L4. Both sample sets were then subject to a tri-layer deposition, Al (4 nm)/Ni₈₁Fe₁₉ (43 nm)/Al (3 nm), to place a protected magnetic coating onto the polymer nanowires within the lattice [Fig. 1(f)]. Deposition of the stack was performed using a thermal evaporator operating at a pressure of 3×10^{-7} mbar. A crystal quartz monitor present during evaporation measured the deposition thickness, which was later confirmed with atomic force microscopy measurements. Sample set B was subject to an oxygen plasma step to further reduce the thickness of the underlying polymer. As shown previously,^{10–12,26} the realized diamond lattice yields an array of single-domain magnetic nanowires that exhibit an Ising-like behavior.

Sample set A was subject to scanning transmission x-ray microscopy (STXM) at Diamond Light Source beamline I08, and sample set B was subject to full-field transmission soft x-ray microscopy (TXM) at the Mistral beamline at ALBA. Prior to data collection at ALBA, x-ray absorption spectra (XAS) were obtained for each sample, and the photon energies corresponding to the L₃ and L₂ peaks of Fe were identified. The samples were first measured in their original as-deposited state. Subsequently, a field of ~ 100 mT was applied using an *ex-situ* permanent magnet. The experimental setup at the ALBA beamline was such that the more convenient measuring protocol was fixing the x-ray beam polarization (to circular left) and acquiring images at absorption edges with opposite dichroic contribution in order to extract the magnetic contrast.³⁵ Approximately 300 images were captured at both Fe L₃ and Fe L₂ photon energies. These images were aligned and normalized against a flat-field image. Flat-field images, obtained without a sample, were systematically acquired immediately before or after sample images

to account for any variations in the x-ray illumination intensity and detector efficiency. This process enabled accurate analysis focused on genuine sample features. Normalized images were converted to optical density (O_D) before an XMCD signal was calculated using

$$\text{XMCD} = L_{3,\text{Fe}} - 2 \cdot L_{2,\text{Fe}}, \quad (1)$$

where $L_{3,\text{Fe}}$ is the O_D image at the Fe L₃ photon energy and $L_{2,\text{Fe}}$ is the O_D image at the Fe L₂ photon energy.

STXM was performed at Diamond Light Source beamline I08. Initially, XAS were obtained by scanning across the Ni- and Fe-L_{2,3} photon energies, allowing for the identification of the specific L_{2,3} edge photon energies associated with each sample. Subsequent data collection involved capturing image stacks using both left- and right-circularly polarized light over the pre-absorption and absorption edges within the energy ranges of Ni (845–885 eV) and Fe (700–723 eV). Optical density images were obtained from the images by using the following relation:

$$O_D = \ln \left(\frac{I_0}{I} \right), \quad (2)$$

where I_0 is the incident photon intensity, determined from sample-free regions of interest, and I is the transmitted intensity. Fe and Ni thickness maps were obtained by analysis of XAS images obtained using STXM at Diamond Light Source and by using the aXis2000 software package.³⁶ Each thickness map was obtained by taking the difference between the optical density image at the pre-edge absorption energy and the relevant resonance absorption peak. To analyze the XAS and estimate the sample thickness, the density and chemical composition of the materials are required. Using the atomic scattering factors available in the tables of Henke *et al.*,³⁷ the absolute thickness can, in principle, be estimated. However, in this work, oxidation limited the extent to which the overall chemical composition and density could be estimated, and thus, we only present the relative change in thickness, sufficient to estimate the wire cross-sectional geometry. XMCD measurements were also attempted using STXM by measurements of images for left- and right-circular polarization, alignment, and subsequent subtraction.

Sample set A was fabricated using a piezo-mode, to provide longer exposures and aid in adhering the written polymer to the substrate surrounding the aperture. Such samples provide maximum stability of the suspended lattice, providing initial feasibility of the transmission-based experiments. Figure 2(a) shows a scanning electron microscopy (SEM) image of the 3DASI lattice, with Fig. 2(b) showing an image taken at 45° tilt. The individual nanowires are found to have widths of 301 ± 7 nm, a length of $1 \mu\text{m}$, and an average thickness of $\sim 1 \mu\text{m}$. Representative XMCD images taken at the Ni L₂ and L₃ edges are shown in Figs. S1(a) and S1(b), respectively, for the region outlined in Fig. 2(a) (dashed lines). Bands of contrast can be seen upon individual nanowires. However, we note that the apparent contrast does not invert between the L₂ image and L₃ image, suggesting that this contrast is not magnetic in origin but likely an artifact. Although XMCD contrast is absent, transmission-based experiments allow the intriguing possibility to explore the 3D cross section of the nanowires in these samples. Previous work has hinted that the wires have a novel crescent-shaped cross section.¹⁰ Figures 2(c) and 2(d) show the thickness maps of the Ni and Fe components of the magnetic material upon the lattice, respectively; both

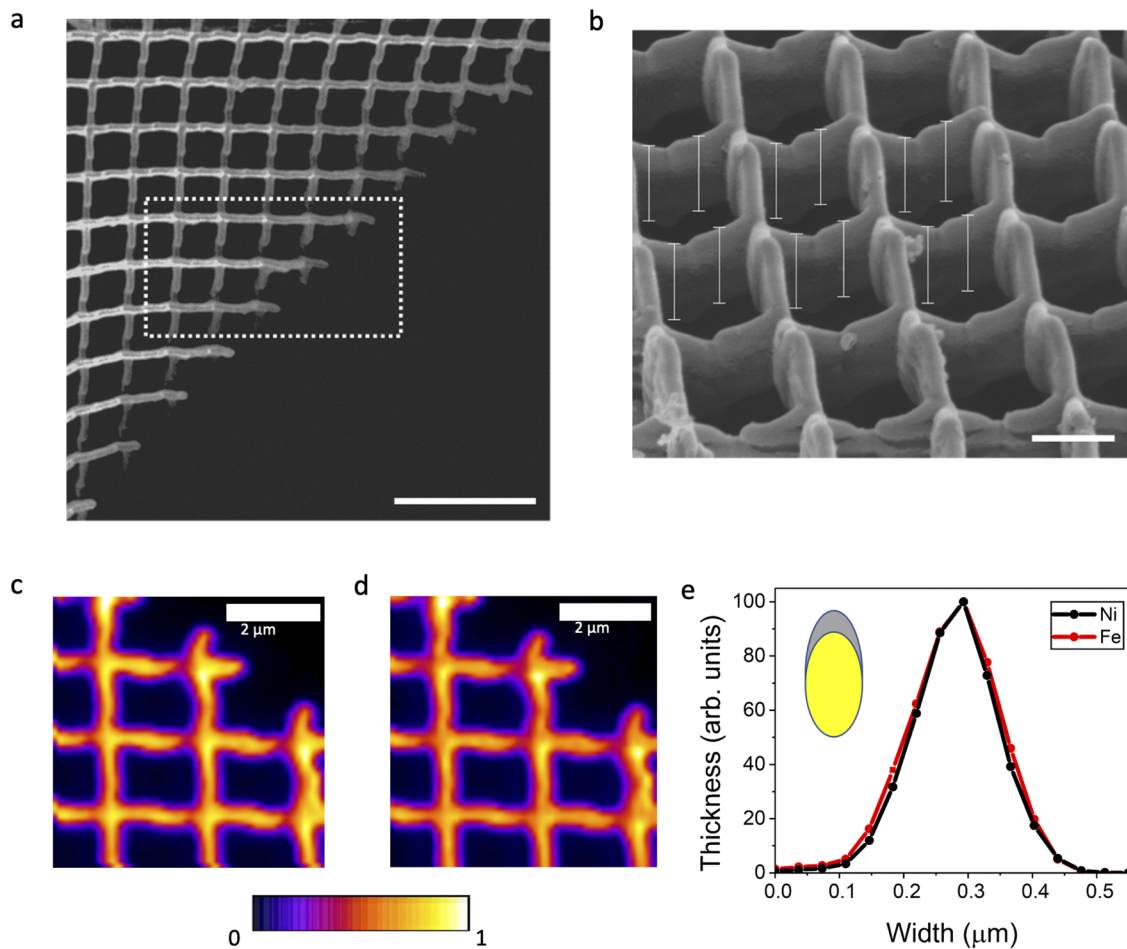


FIG. 2. Determination of magnetic nanowire cross section. (a) Scanning electron microscopy image of the sample measured at Diamond Light Source. The region where XMCD was measured is outlined by the dotted line. The scale bar shown is 5 μm . (b) SEM image of the 3DASI viewed from a 45° tilt. Annotated measurements show regions of wires measured for thickness measurements. A trigonometry calculation was used to transform measured values to account for the tilt in image. An average thickness of 1.03 μm is obtained. The scale shown is 1 μm . (c) Heat map of Ni thickness. (d) Heat map of Fe thickness. (e) Average Ni and Fe cross-sectional thickness profiles, across 16 measured lattice nanowires. Inset: the elliptical cross section of a TPL voxel (yellow) and the crescent shaped cross section of NiFe (gray) obtained when adding a graded thickness, as suggested by the measured thickness heat maps.

show that the magnetic material is uniform across much of the lattice with a region of decreased thickness found at the intersection of SL1 and SL2. In this location, the measured optical density drops by 40%. This can be explained with SEM measurements, which show that the suspended lattice tilts slightly into the aperture, which combined with the evaporation at a normal incidence to the sample will result in a change in deposition thickness transverse to the tilt axis. Extracting line profiles across the wire width allows the cross-sectional thickness variation to be determined, as shown in Fig. 2(e). The profile shows a graded thickness as previously hinted by SEM imaging.¹⁰ When considering the cross-sectional geometry of a TPL voxel, which has an elliptical shape,²⁶ the superposition of a graded NiFe thickness yields wires of crescent-shaped cross section, as shown in the inset of Fig. 2(e). Magnetic nanowires with a crescent-shaped cross section are expected to host domain walls

with perturbed spin textures due to the curvature yielding effective anisotropy and Dzyaloshinskii–Moriya energies.¹⁶ Overall, initial STXM studies conducted at Diamond Light Source on sample set A provided feasibility of measurement and gave insight into the physical cross section of the nanowires.

Sample set B was fabricated with galvanometric mirrors, which reduced the exposure dose of the lattice. A key advantage of this approach is a reduced thickness of the polymer nanowires. Exposure to oxygen plasma further reduces the polymer thickness. A SEM image of a suspended 3DASI from sample set B is shown in Fig. 3(a), with high magnification images shown in Figs. 3(b) and 3(c). Nanowires were found to have widths of $\sim 220 \pm 6$ nm and lengths of 1 μm . Atomic force microscopy (AFM) was used to measure surface topography, as shown in Fig. 3(d). The 3DASI in this sample set comprises four sub-lattice layers designated SL1

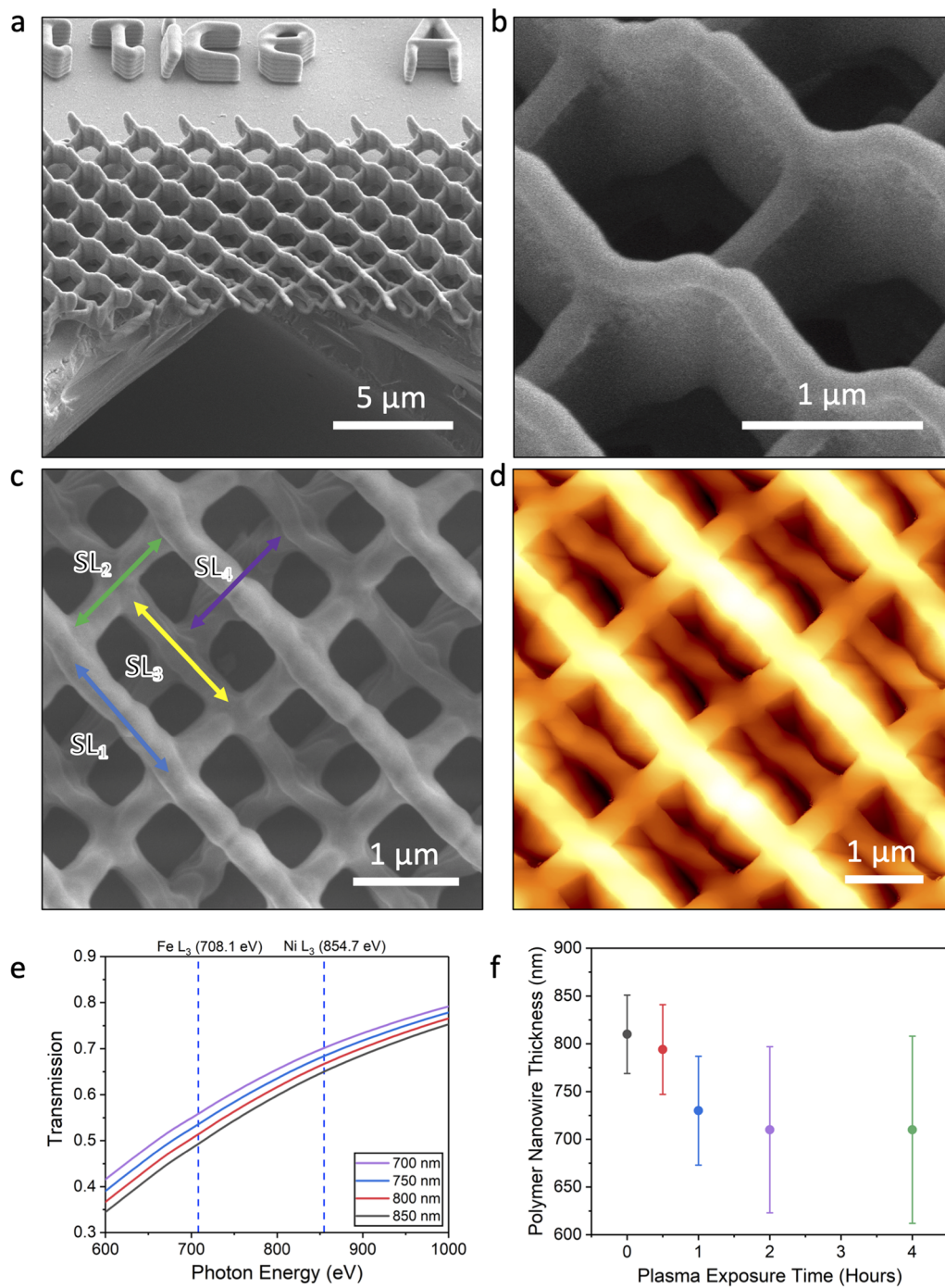


FIG. 3. A multiple layer suspended 3DASI lattice. (a) Scanning electron microscopy image (SEM) of the 3DASI lattice suspended over an aperture corner. (b) Zoomed-in SEM image of the upper surface. (c) Top-view SEM of the suspended lattice. Sub-lattices of different depths are labeled SL₁ (highest), SL₂, SL₃, and SL₄ (lowest). (d) Atomic force microscopy image for region of the suspended 3DASI lattice. (e) Calculated transmission of x rays through PMMA ($\text{C}_5\text{H}_8\text{O}_2$) for different values of polymer thickness, as indicated in the legend. The Fe and Ni L₃ edges are shown at the top of the panel. Transmission calculations were carried out using the center of x-ray optics online tool, with PMMA as the approximate resist material. (f) Average polymer scaffold thickness measured via tilted SEM micrographs plotted against oxygen plasma exposure. A $\sim 10\%$ drop was measured in scaffold thickness for 60 min plasma exposure with diminishing returns for further exposure. The standard deviation of wire thickness increases with greater plasma exposure time due to non-uniform exposure across wires.

through to SL4, as depicted in Fig. 3(c). The average thickness of the nanowires for this sample set was found to be $\sim 810 \pm 18$ nm, which is lower than that of sample set A.

The transmission (T) of x rays through the polymer layer can be determined using³⁷

$$T = \exp(-n\mu_a d), \quad (3)$$

where d is the thickness of the layer, n is the density, and μ_a is the atomic photo-absorption cross section, which is defined as

$$\mu_a = 2r_0\lambda f_2, \quad (4)$$

where r_0 is the classical electron radius, λ is the wavelength, and f_2 is the imaginary component of the atomic scattering factor. Based on the Henke tables, estimates of x-ray transmission through the polymer for sample set B suggested a transmission of 65% at the Ni L_3 edge photon energy and 51% at the Fe L_3 edge photon energy, as shown in Fig. 3(e) (black line). We calculate that a 100 nm thick Si_3N_4 membrane has a transmission of $\sim 80\%$ – 85% at the Fe L_3 edge photon energy. The increased polymer thickness present in our structures adds substantially to the non-magnetic background and will, therefore, reduce the signal-to-noise of XMCD measurements. In an attempt to circumvent this problem, a sample set was fabricated with increasing oxygen plasma exposure time. The oxygen plasma selectively removes the carbon-based polymer, reducing its thickness and increasing soft x-ray transmission, as shown in Figs. 3(e) and 3(f). In these structures, the process appears to be self-limiting, with an exponential-like decay in the polymer thickness. Previous work on simple polymer-based scaffolds has suggested a similar trend, whereby the etch rate was found to be high (~ 12 nm per minute) in the first 2 min, to almost no observable etching after

6 min.³⁹ We note that in our structure, the stray field from the magnetic coating may also shield structures from the plasma, reducing the overall etching performance.

Sample set B was measured using in-house magneto-optical Kerr effect (MOKE) magnetometry prior to x-ray microscopy measurements. MOKE loops upon the Si substrate that surrounds the aperture yielded a hysteresis loop with a coercive field of $\mu_0 H_C = 0.6$ mT as-deposited and 0.5 mT after a 30 min plasma exposure, as shown in Fig. S2 of the supplementary material. The slightly increased coercivity is likely due to the substrate roughness or slight oxidation but is still consistent with the range measured previously³⁸ for evaporated $\text{Ni}_{81}\text{Fe}_{19}$. Figure 4(a) shows the XAS taken at the Fe L_3 edge upon samples with varying oxygen plasma exposure, with the full spectra shown in Fig. S3 of the supplementary material. The sample with no oxygen plasma exposure shows a peak at 707.5 eV, indicating metallic $\text{Ni}_{81}\text{Fe}_{19}$. The presence of a shoulder at ~ 709 eV suggests some oxidation,⁴⁰ despite a capping layer. Measurement of samples with increasing oxygen exposure yields more evidence of a multiplet structure with increasing peak intensity at ~ 709 eV. The inset of Fig. 4(a) shows that the ratio of Fe peak to Fe_3O_4 peak decreases with increasing oxygen plasma exposure time. Overall, these results suggest that samples with an intermediate oxygen plasma exposure time will have the best balance of a reduced polymer thickness but with a large volume fraction of metallic $\text{Ni}_{81}\text{Fe}_{19}$. Specifically, for the 60-min oxygen plasma exposure, the polymer thickness is reduced by $\sim 10\%$. This should yield an improved transmission while maintaining a Fe/ Fe_3O_4 L_3 peak ratio of 0.95.

Figure 4(b) shows an XAS optical density image taken at the Fe L_3 edge upon a sample that was exposed to oxygen plasma for the optimal 60 min. A crucial uncertainty with respect to such samples was the extent to which the 3DASI structure, which is suspended,

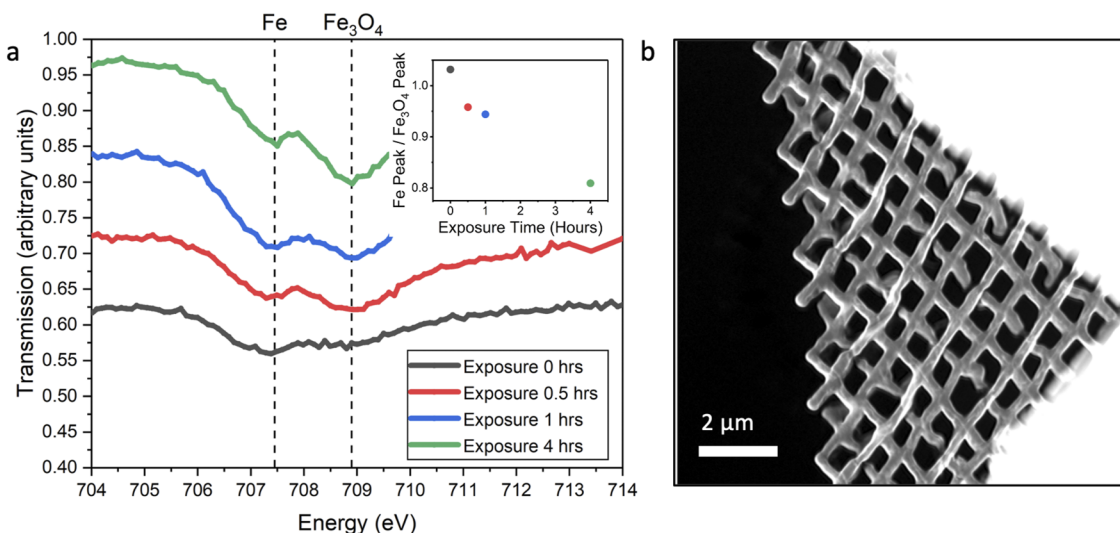


FIG. 4. Determining optimal processing parameters for soft x-ray microscopy. (a) Fe L_3 spectra for samples of increasing oxygen exposure time. Each spectrum is the average across wires on the lattice. The spectra have been artificially offset in the vertical axis for clarity. The Fe L_3 absorption edge presents an oxidized component that appears as a shoulder peak at 709 eV with intensity dependent on the oxygen plasma exposure time. The inset shows the ratio of metallic peak to oxide peak, as a function of plasma exposure time. (b) Optical density image at the Fe L_3 photon energy of a suspended 3DASI lattice.

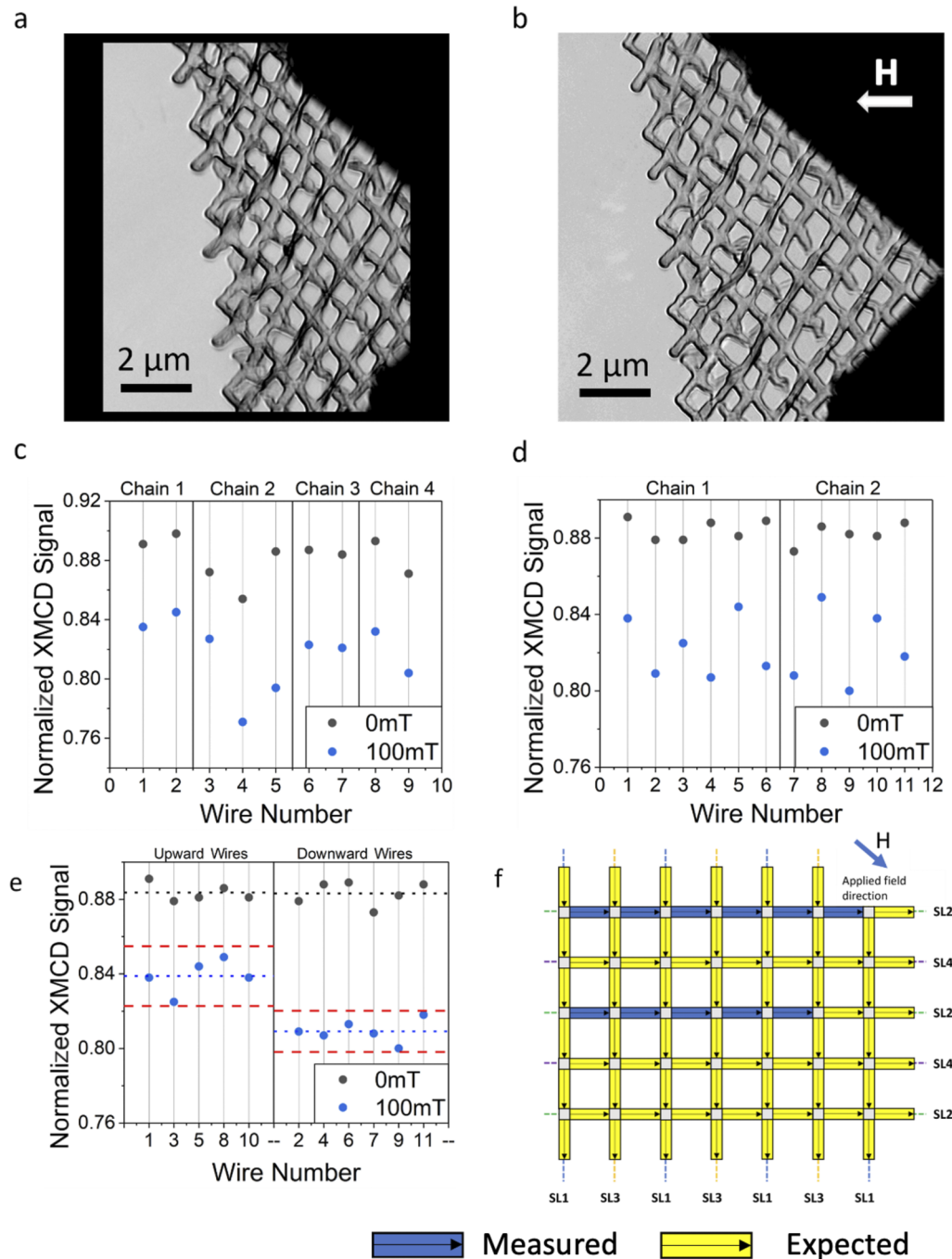


FIG. 5. Measurement of magnetic contrast upon a suspended 3D artificial spin ice. (a) X-ray Magnetic Circular Dichroism (XMCD) image of the lattice in the as-deposited state and (b) after the application of a 100 mT field, in the direction indicated by the white arrow. (c) Normalized XMCD signal for wire chains in the as-deposited state (gray circles) and after the application of a 100 mT field (blue circles), for the SL1 sub-lattice. (d) Normalized XMCD signal for wire chains in the as-deposited state (gray circles) and after the application of a 100 mT field (blue circles), for the SL2 sub-lattice. (e) Extracted XMCD contrast for nanowires upon the SL2 sub-lattice, for magnetization of different tilts with respect to incoming wavevector. After saturation, magnetization of different tilt signs are expected to have distinct XMCD contrast since they have opposing M_z components. The gray symbols indicate XMCD signals for nanowires before the application of a field, and the blue symbols represent XMCD signals after the application of the field. In each case, the blue dotted lines represent the mean of the populations, while the dashed lines represent the 2σ boundary. There is no overlap in populations to within 2σ . (f) Schematic of the extracted magnetization contrast from XMCD measurements. The blue dashed line labels the SL1 sub-lattice, the green dashed line labels the SL2 sub-lattice, the yellow dashed line indicates the SL3 sub-lattice, and the purple dashed line labels the SL4 sub-lattice. The measured magnetic nanowires are colored in blue, while the yellow wires show the expected configuration given the applied field direction.

fabricated using Galvanometric mirrors with reduced anchoring, and subject to oxygen plasma, would remain stable. Analysis of multiple images taken over several hours, as shown in Supplementary Video 1, shows little movement or distortion of the lattice. Some regions within Fig. 4(b) can be clearly seen to have higher x-ray absorption. In many cases, these areas are correlated with overlap in lower structures.

Figure 5 shows the XMCD images using TXM, of a lattice subject to a 60-min oxygen plasma exposure, in an as-deposited state [Fig. 5(a)] and after the application of a 100 mT field [Fig. 5(b)]. An apparent contrast is present in the images, with dark regions particularly noticeable at the vertices. A close inspection of these regions suggests that this contrast is not of magnetic origin but due to overlapping features. To carefully inspect the measurement for evidence of magnetism, non-overlapping regions were found and chains, connected wires on a specific sub-lattice, were identified for SL1, SL2, and SL3, as shown in Fig. S4 of the supplementary material. The average XMCD signal for Fe L_3 across the central region of the wire, where there is a negligible structural background, was measured. This was then plotted for each of the three wire sub-lattices for the as-deposited state and after the application of a 100 mT magnetic field, as shown in Figs. 5(c) and 5(d). Previous studies have shown the magnetic configuration that would be expected after the application of a saturating field.¹² In-plane saturation along each of the sub-lattices will yield a net magnetization component parallel to the field. However, since each wire along a given sub-lattice has an alternating $\pm 35.25^\circ$ angle, out of the substrate plane, and since XMCD measurements are sensitive to the magnetization component along the photon propagation direction, for a saturated sample, we expect to see alternating contrast as depicted in Fig. S5 of the supplementary material. An examination of the SL1 chain contrast, as shown in Fig. 5(c), yields inconclusive results. Since the uppermost layer is most susceptible to artifacts due to overlap, only short chains can be identified, and these do not show a difference in trend when comparing configurations before and after field application. This suggests that any XMCD signal upon the SL1 sub-lattice is below the noise floor of the measurement. Analysis of data upon SL2, shown in Fig. 5(d), is more intriguing. The relative contrast, wire-to-wire, is different before and after the application of the magnetic field. Notably, the chain data after the application of a magnetic field take the expected form with alternating contrast, as depicted in Fig. S5 of the supplementary material. The XMCD signal is weak, at around 4%, likely due to a reduced magnetic moment driven by oxidation. An alternative analysis that can be performed is to inspect the magnitude of the contrast for wires in adjacent chains. Here, we expect wires with positive and negative magnetization projections onto k to have distinct values. Figure 5(e) shows the XMCD signal for the two sets of wires before and after the application of a field. Before the application of the field, the average XMCD value for both sets of wires are found to be within 0.5%, suggesting a net out-of-plane magnetization. After the application of the field, both SL2 and SL3 had a difference of $\sim 4\%$, consistent with the previous analysis, suggesting the presence of a weak magnetic signal. However, only SL2 has distinct populations of the XMCD signal, for which there is no overlap within 2σ , suggesting high confidence in magnetic contrast. Plotting the magnetization of the SL2, as shown in Fig. 5(f),

also shows that the measured configuration is consistent with the direction of the external field, providing additional confidence. We note that similar analysis on SL3 shows weaker evidence of magnetic contrast, as shown in Figs. S6 and S7 of the supplementary material. Although there is a difference in the mean XMCD signal between upward and downward wires, there is a strong overlap in the two populations. We note that it is possible for a small drift in focus to account for the small XMCD signals observed on the SL2 and SL3 sub-lattices, but that this would impact all sub-lattices, whereas for SL1 [Fig. 5(a)], there is clearly no change in the trend before and after field application. Additional comparative analysis of wire widths (SL1, SL2, and SL3), shown in Fig. S8 of the supplementary material, between XAS images of pre-field and post-field applications revealed consistent measurements within the margin of error, suggesting a negligible drift in focus.

A key question is why only specific sub-lattices within the structure show evidence of magnetic contrast. The oxygen plasma exposure is expected to be uniform across ~ 100 mm diameter. However, the extent to which the plasma can penetrate a $50 \times 50 \mu\text{m}^2$ aperture is less certain. Furthermore, the stray field lines from the NiFe coating may partially shield the lattice, particularly the lower layers. This may impact both the extent to which different sub-lattices have oxidized NiFe and the resulting gradient in polymer thickness when going from SL1 to SL4 sub-lattices. Overall, this is likely to lead to a trend whereby SL1 has the most polymer removed but also has the most prominent reduction in magnetization due to oxidation. At the other extreme, SL3 and SL4 are likely to have a higher magnetization but the least polymer removed, yielding a lower signal-to-noise ratio in XMCD measurements. Then, the intermediate SL2 sub-lattice is likely to be optimal in terms of magnetization and polymer removal.

In conclusion, a 3DASI lattice has been fabricated over an aperture using two-photon lithography, deposition, and oxygen plasma exposure. The 3D lattice is found to be stable when subject to repeated soft x-ray exposure. The plasma exposure of the polymer scaffold improved x-ray transmission through the structure, yielding a greater signal than would otherwise be seen. XAS data are used to extract the cross section of the magnetic nanowire, which is found to take a novel crescent-shaped geometry. XMCD measurements suggest that a signal can be measured on the buried sub-lattices, hinting at the expected configuration after an applied field. Minor adjustments in the fabrication procedure, by using a shorter wavelength laser,⁴¹ are expected to reduce the need for oxygen plasma and, when combined with optimized beamline measurement protocols, are expected to provide uniform magnetic contrast across all lattice layers and an improved signal to noise ratio.

S.L. acknowledges the funding from the Engineering and Physics Research Council (Grant Nos. EP/X012735/1 and EP/R009147/1) and the Leverhulme Trust (Grant No. RPG-2021-139). D.R. and P.F. were supported by U.S. Department of Energy, Office of Science, Office of Basic Energy Sciences, Materials Sciences and Engineering Division under Contract No. DE-AC02-05-CH11231 (NEMM program MSMAG).

AUTHOR DECLARATIONS

Conflict of Interest

The authors have no conflicts to disclose.

Author Contributions

Edward Harding: Conceptualization (equal); Data curation (equal); Formal analysis (equal); Funding acquisition (equal); Investigation (equal); Methodology (equal); Project administration (equal); Supervision (equal); Writing – original draft (equal). **Tohru Araki:** Data curation (equal); Formal analysis (equal); Investigation (equal); Methodology (equal); Writing – original draft (equal); Writing – review & editing (equal). **Joseph Askey:** Data curation (equal); Formal analysis (equal); Investigation (equal); Methodology (equal); Writing – review & editing (equal). **Matthew Hunt:** Conceptualization (equal); Formal analysis (equal); Funding acquisition (equal); Investigation (equal); Writing – review & editing (equal). **Arjen Van Den Berg:** Data curation (equal); Formal analysis (equal); Investigation (equal); Methodology (equal); Writing – review & editing (equal). **David Raftrey:** Formal analysis (equal); Investigation (equal); Writing – review & editing (equal). **Lucia Aballe:** Data curation (equal); Formal analysis (equal); Investigation (lead); Methodology (equal); Writing – review & editing (equal). **Burkhard Kaulich:** Funding acquisition (equal); Investigation (equal); Methodology (equal); Writing – review & editing (equal). **Emyr MacDonald:** Formal analysis (equal); Investigation (equal). **Peter Fischer:** Conceptualization (equal); Formal analysis (equal); Funding acquisition (equal); Investigation (equal); Writing – review & editing (equal). **Sam Ladak:** Conceptualization (equal); Funding acquisition (equal); Investigation (equal); Methodology (equal); Project administration (equal); Supervision (equal).

DATA AVAILABILITY

The data that support the findings of this study are openly available in the Cardiff University data catalog at <http://doi.org/10.17035/d.2024.0305551299>.

REFERENCES

- A. Fernández-Pacheco, R. Streubel, O. Fruchart, R. Hertel, P. Fischer, and R. P. Cowburn, *Nat. Commun.* **8**(1), 15756 (2017).
- P. Fischer, D. Sanz-Hernández, R. Streubel, and A. Fernández-Pacheco, *APL Mater.* **8**(1), 010701 (2020).
- D. Makarov, O. Volkov, A. Kakay, O. Pylypovskiy, B. Budinska, and O. Dobrovolskiy, *Adv. Mater.* **34**(3), 2101758 (2022).
- D. Raftrey, A. Hierro-Rodríguez, A. Fernandez-Pacheco, and P. Fischer, *J. Magn. Magn. Mater.* **563**, 169899 (2022).
- S. S. P. Parkin, M. Hayashi, and L. Thomas, *Science* **320**(5873), 190–194 (2008).
- K. Gu, Y. Guan, B. K. Hazra, H. Deniz, A. Migliorini, W. Zhang, and S. P. Parkin, *Nat. Nanotechnol.* **17**, 1065–1071 (2022).
- J. Llandro, D. M. Love, A. Kovács, J. Caron, K. N. Vyas, A. Kákay, R. Salikhov, K. Lenz, J. Fassbender, M. R. J. Scherer, C. Ciorra, U. Steiner, C. H. W. Barnes, R. E. Dunin-Borkowski, S. Fukami, and H. Ohno, *Nano Lett.* **20**(5), 3642–3650 (2020).
- D. Sanz-Hernandez, A. Hierro-Rodríguez, C. Donnelly, J. Pablo-Navarro, A. Sorrentino, E. Pereiro, C. Magen, S. McVitie, J. de Teresa, S. Ferrer, P. Fischer, and A. Fernandez-Pacheco, *ACS Nano* **14**(7), 8084–8092 (2020).
- C. Donnelly, A. Hierro-Rodríguez, C. Abert, K. Witte, L. Skoric, D. Sanz-Hernández, S. Finizio, F. Meng, S. McVitie, J. Raabe, D. Suess, R. Cowburn, and A. Fernández-Pacheco, *Nat. Nanotechnol.* **17**(2), 136–142 (2022).
- A. May, M. Hunt, A. Van Den Berg, A. Hejazi, and S. Ladak, *Commun. Phys.* **2**(1), 13 (2019).
- A. Van Den Berg, M. Caruel, M. Hunt, and S. Ladak, *Nano Res.* **16**(1), 1441–1447 (2023).
- A. May, M. Saccone, A. Van Den Berg, J. Askey, M. Hunt, and S. Ladak, *Nat. Commun.* **12**(1), 3217 (2021).
- S. Sahoo, S. Mondal, G. Williams, A. May, S. Ladak, and A. Barman, *Nanoscale* **10**(21), 9981–9986 (2018).
- S. Sahoo, A. May, A. van Den Berg, A. K. Mondal, S. Ladak, and A. Barman, *Nano Lett.* **21**(11), 4629–4635 (2021).
- Y. Gaididei, A. Goussev, V. P. Kravchuk, O. V. Pylypovskiy, J. M. Robbins, D. D. Sheka, V. Slastikov, and S. Vasylykevych, *J. Phys. A: Math. Theor.* **50**(38), 385401 (2017).
- Y. Gaididei, V. P. Kravchuk, and D. D. Sheka, *Phys. Rev. Lett.* **112**(25), 257203 (2014).
- D. D. Sheka, O. V. Pylypovskiy, O. M. Volkov, K. V. Yershov, V. P. Kravchuk, and D. Makarov, *Small* **18**(12), 2105219 (2022).
- V. P. Kravchuk, U. K. Rößler, O. M. Volkov, D. D. Sheka, J. van den Brink, D. Makarov, H. Fuchs, H. Fangohr, and Y. Gaididei, *Phys. Rev. B* **94**(14), 144402 (2016).
- O. V. Pylypovskiy, D. D. Sheka, and Y. Gaididei, *Phys. Rev. B* **85**(22), 224401 (2012).
- V. P. Kravchuk, D. D. Sheka, A. Kákay, O. M. Volkov, U. K. Rößler, J. van den Brink, D. Makarov, and Y. Gaididei, *Phys. Rev. Lett.* **120**(6), 067201 (2018).
- K. V. Yershov, V. P. Kravchuk, D. D. Sheka, O. V. Pylypovskiy, D. Makarov, and Y. Gaididei, *Phys. Rev. B* **98**(6), 060409 (2018).
- M. Vazquez, *J. Magn. Magn. Mater.* **543**, 168634 (2022).
- R. Streubel, D. J. Thurmer, D. Makarov, F. Kronast, T. Kosub, V. Kravchuk, D. D. Sheka, Y. Gaididei, R. Schäfer, and O. G. Schmidt, *Nano Lett.* **12**(8), 3961–3966 (2012).
- D. Yeon Nam, A. Y. Samardak, Y. S. Jeon, S. H. Kim, A. V. Davydenko, A. V. Ognev, A. S. Samardak, and Y. K. Kim, *Nanoscale* **10**, 20405–20413 (2018).
- C. Phatak, C. S. Miller, Z. Thompson, E. B. Gulsoy, and A. K. Petford-Long, *ACS Appl. Nano Mater.* **3**(6), 6009–6016 (2020).
- M. Hunt, M. Taverne, J. Askey, A. May, A. Van Den Berg, Y.-L. D. Ho, J. Rarity, and S. Ladak, *Materials* **13**(3), 761 (2020).
- A. Fernández-Pacheco, L. Serrano-Ramón, J. M. Michalik, M. R. Ibarra, J. M. De Teresa, L. O'Brien, D. Petit, J. Lee, and R. P. Cowburn, *Sci. Rep.* **3**(1), 1492 (2013).
- J. M. De Teresa, A. Fernández-Pacheco, R. Córdoba, L. Serrano-Ramón, S. Sangiao, and M. R. Ibarra, *J. Phys. D: Appl. Phys.* **49**(24), 243003 (2016).
- D. Sanz-Hernandez, R. F. Hamans, J. W. Liao, A. Welbourne, R. Lavrijsen, and A. Fernandez-Pacheco, *ACS Nano* **11**(11), 11066–11073 (2017).
- S. Gliga, G. Seniutinas, A. Weber, and C. David, *Mater. Today* **26**, 100–101 (2019).
- C. Donnelly, M. Guizar-Sicairos, V. Scagnoli, M. Holler, T. Huthwelker, A. Menzel, I. Vartiainen, E. Müller, E. Kirk, S. Gliga, J. Raabe, and L. J. Heyderman, *Phys. Rev. Lett.* **114**(11), 115501 (2015).
- P. Pip, S. Treves, J. R. Massey, S. Finizio, Z. Luo, A. Hrabec, V. Scagnoli, J. Raabe, L. Philippe, L. J. Heyderman, and C. Donnelly, *APL Mater.* **10**(10), 101101 (2022).
- R. Streubel, P. Fischer, F. Kronast, V. Kravchuk, D. Sheka, Y. Gaididei, O. Schmidt, and D. Makarov, *J. Phys. D Appl. Phys.* **49**, 363001 (2016).
- T. Srivastava, Y. Sassi, F. Ajejas, A. Vecchiola, I. Ngouagna Yemeli, H. Hurdequint, K. Bouzehouane, N. Reyren, V. Cros, T. Devolder, J.-V. Kim, and G. de Loubens, *APL Mater.* **11**(6), 061110 (2023).
- J. A. Fernandez-Roldan, C. Bran, A. Asenjo, M. Vázquez, A. Sorrentino, S. Ferrer, O. Chubykalo-Fesenko, and R. P. del Real, *Nanoscale* **14**(37), 13661–13666 (2022).

³⁶A. P. Hitchcock, *J. Electron Spectrosc. Relat. Phenom.* **266**, 147360 (2023).

³⁷B. Henke, E. Gullikson, and J. Davis, *At. Data Nucl. Data Tables* **54**(2), 181–342 (1993).

³⁸A. Guittoum, A. Bourzami, A. Layadi, and G. Schmerber, *Eur. Phys. J.: Appl. Phys.* **58**(2), 20301 (2012).

³⁹G. Seniutinas, A. Weber, C. Padeste, I. Sakellari, M. Farsari, and C. David, *Microelectron. Eng.* **191**, 25–31 (2018).

⁴⁰T. J. Regan, H. Ohldag, C. Stamm, F. Nolting, J. Lüning, J. Stöhr, and R. L. White, *Phys. Rev. B* **64**(21), 214422 (2001).

⁴¹P. Mueller, M. Thiel, and M. Wegener, *Opt. Lett.* **39**, 6847 (2014).